HAL open science

Polymerization of glycidyl methacrylate from the surface of cellulose nanocrystals for the elaboration of PLA-based nanocomposites

Manon Le Gars, Julien Bras, Hanène Salmi-Mani, Marisol Ji, Diana Dragoe, Sandra Domenek, Hajar Faraj, Naceur Belgacem, Philippe Roger

To cite this version:

Manon Le Gars, Julien Bras, Hanène Salmi-Mani, Marisol Ji, Diana Dragoe, et al.. Polymerization of glycidyl methacrylate from the surface of cellulose nanocrystals for the elaboration of PLA-based nanocomposites. Carbohydrate Polymers, 2020, 234, pp.115899. 10.1016/j.carbpol.2020.115899 . hal-03322807

HAL Id: hal-03322807

https://hal.science/hal-03322807

Submitted on 21 Jul 2022

HAL is a multi-disciplinary open access archive for the deposit and dissemination of scientific research documents, whether they are published or not. The documents may come from teaching and research institutions in France or abroad, or from public or private research centers.

L'archive ouverte pluridisciplinaire **HAL**, est destinée au dépôt et à la diffusion de documents scientifiques de niveau recherche, publiés ou non, émanant des établissements d'enseignement et de recherche français ou étrangers, des laboratoires publics ou privés.

Distributed under a Creative Commons Attribution - NonCommercial 4.0 International License

Version of Record: https://www.sciencedirect.com/science/article/pii/S0144861720300734
Manuscript_31495e8bb36578f2d001262579a19f8f

Polymerization of glycidyl methacrylate from the surface of cellulose nanocrystals for the elaboration of PLA-based nanocomposites

Manon Le Gars [a] (manon.le-gars@lgp2.grenoble-inp.fr), **Julien Bras** [a] (julien.bras@grenoble-inp.fr), **Hanène Salmi-Mani** [b] (hanene.salmi@u-psud.fr), **Marisol Ji** [b] (mji1119@hotmail.com), **Diana Dragoe** [b] (diana.dragoe@u-psud.fr), **Hajar Faraj** [c] (hajar.faraj@agroparistech.fr), **Sandra Domenek** [c] (sandra.domenek@agroparistech.fr), **Naceur Belgacem** [a, d] (naceur.belgacem@pagora.grenoble-inp.fr), **Philippe Roger** [b, 1] (philippe.roger@u-psud.fr)

[a] *Univ. Grenoble Alpes, CNRS, Grenoble INP*[2]*, LGP2, F-38000 Grenoble, France*

[b] *Institut de Chimie Moléculaire et des Matériaux d'Orsay (ICMMO), UMR 8182, Université Paris Sud, CNRS, Université Paris-Saclay, 91405 Orsay, France*

[c] *UMR Ingénierie Procédés Aliments, AgroParisTech, INRA, Université Paris Saclay, F-91300 Massy, France*

[d] *Institut Universitaire de France (IUF), 75000 Paris, France*

Abstract

Cellulose nanocrystals (CNCs) are used to design nanocomposites because of their high aspect ratio and their outstanding mechanical and barrier properties. However, the low compatibility of hydrophilic CNCs with hydrophobic polymers remains a barrier to their use in the nanocomposite field. To improve this compatibility, poly(glycidyl methacrylate) (PGMA) was grafted from CNCs containing α-bromoisobutyryl moieties *via* surface-initiated atom transfer radical polymerization. The novelty of this research is the use of a reactive epoxy-containing monomer that can serve as a new platform for further modifications or crosslinking. Polymer-grafted CNC-PGMA-Br prepared at different polymerization times were characterized by XRD, DLS, FTIR, XPS and elemental analysis. Approximately 40% of the polymer at the surface of the CNCs was quantified after only 1 h of

[1] **Corresponding author** : Université Paris-Sud, 15 rue Georges Clémenceau, 91405 Orsay Cedex, France, +33 1 69 15 47 16

[2] *Institute of Engineering Univ. Grenoble Alpes*

© 2020 published by Elsevier. This manuscript is made available under the CC BY NC user license
https://creativecommons.org/licenses/by-nc/4.0/

polymerization. Finally, nanocomposites prepared with 10 wt% CNC-PGMA-Br as nanofillers in a poly(lactic acid) (PLA) matrix exhibited an improvement in their compatibilization based on SEM observation.

Keywords: Cellulose nanocrystals; Chemical grafting; Surface-initiated atom transfer radical polymerization; Poly(glycidyl methacrylate); Poly(lactic acid)-based nanocomposites; Compatibilization

1. Introduction

Because of its abundance and availability from a wide variety of sources, cellulose is currently a polymer of choice in the field of bio-based materials. Recently, several novel nanomaterials have been extracted from this natural biopolymer. Indeed, cellulose nanofibrils (CNFs) have been classically obtained since the 1980s by applying a mechanical treatment to a cellulose suspension (Nechyporchuk et al., 2016). Conversely, since the 1960s, CNCs are produced by performing an acid hydrolysis, meaning removing the amorphous part of cellulose (Habibi et al., 2010; Kargarzadeh et al., 2018). Such nanomaterials are relevant for a large number of research fields, like nanocomposites (Ferreira et al., 2017; Habibi, 2014; Kargarzadeh et al., 2018; Oksman et al., 2016), coatings (Ferrer et al., 2017; Hubbe et al., 2017), packaging (Ferrer et al., 2017; Hubbe et al., 2017), and biomedical applications (Domingues et al., 2014; Jorfi & Foster, 2015; Lin & Dufresne, 2014). They exhibit interesting properties like biodegradability, renewability, and mechanical and barrier properties that endow them with particular advantages. In the past decade, accelerated industrialization and commercialization of such cellulosic nanomaterials has occurred, in parallel with an ever-increasing demand from industry.

Among nanocelluloses, CNCs exhibit interesting properties. Acid hydrolysis of native cellulose from various sources (cotton, wood, natural fibres, etc.) using sulfuric acid H_2SO_4 leads to CNCs with different dimensions and aspect ratios. The resulting sulfuric-acid-hydrolyzed CNCs hold sulfate half ester groups ($-OSO_3^-$) on their surface (Beck et al., 2015; Foster et al., 2018), with a surface charge density generally in the range from 80 to 350 $\mu mol.g^{-1}$ (Foster et al., 2018; Reid et al., 2016). These surface charges combined with their nanometric size — 150-500 nm in length (up to 1000 nm), 5-20 nm in width according to their source (Foster et al., 2018; Kargarzadeh et al., 2018) — induce colloidal stability of aqueous suspensions (Beck et al., 2015; Foster et al., 2018). In addition to their high aspect ratio, CNCs exhibit a high surface area (Foster et al., 2018; Natterodt et al., 2017), high crystallinity (Klemm et al., 2011), and a large availability of hydroxyl groups on their surface (Foster et al., 2018; Natterodt et al., 2017). Moreover, their rod-like shape, their high mechanical strength (Young's modulus between 120 and 200 GPa) (Dufresne, 2018; Lin et al., 2012), and their sustainability make them attractive materials as fillers in nanocomposites (Boujemaoui et al., 2017; E. Espino-Pérez et al., 2016; Etzael Espino-Pérez et al., 2018; Oksman et al., 2016).

However, the hydrophilicity of CNCs ─ resulting from the three OH groups per anhydroglucose unit (AGU) ─ limits their dispersion in several polymer matrices, especially non-polar matrices. Moreover, CNCs begin to degrade at approximately 200-300°C (Moon et al., 2011), depending on their

morphology, crystallinity, and source. These two last points are challenging when such nanomaterials are used for nanocomposite processing, where high temperatures are reached with expected well-dispersed nanofillers (Belgacem, 2008; Siqueira, Bras, & Dufresne, 2010). These challenges can be overcome through chemical or physico-chemical modifications of CNCs (Eyley & Thielemans, 2014; Habibi, 2014; Natterodt et al., 2017), by grafting single molecules (de Castro et al., 2016; Etzael Espino-Pérez et al., 2014; Eyley & Thielemans, 2014) or polymers chains (Azzam et al., 2010; Boujemaoui et al., 2017; Goffin et al., 2011) at the surface of CNCs, or by adsorbing various molecules, involving ionic or low-energy bonding phenomena (Abitbol, 2014; Kargarzadeh et al., 2018; Kedzior et al., 2017).

Chemical modifications are carried out by modifying multiple hydroxyl groups at the surface of CNCs to provide the nanomaterials with specific properties. To improve the compatibility of CNCs with a hydrophobic polymer matrix, grafting single molecules or polymer chains are classically described in the literature and in reviews. Focusing on the second strategy, two major approaches are commonly used to introduce polymeric chains at the surface of CNCs. In the *grafting-onto* strategy, CNCs, ether pre-functionalized or not, are directly grafted with previously polymerized and characterized polymer chains (Kloser & Gray, 2010; Sessini et al., 2018; Zhou et al., 2018), leading to limited surface grafting density because of the steric hindrance between polymers. In the *grafted-from* approach — on which this study focuses — monomers are polymerized from pre-functionalized CNCs with initiator sites (Boujemaoui et al., 2017; Habibi et al., 2008; Morandi et al., 2009). This two-step strategy leads to an overall controlled structure and higher surface grafting density because of the facilitated access to the activated initiator sites on CNCs, although characterization of grafted polymer chains is more challenging (Zhang et al., 2018). Ring-opening polymerization (ROP) (Goffin et al., 2011; Habibi et al., 2008) and atom transfer radical polymerization (ATRP) (Kedzior et al., 2016; Morandi et al., 2009; Zoppe et al., 2010) are the most common types of polymerization used in the *grafting-from* strategy. Controlled surface-initiated ATRP (SI-ATRP) from the surface of CNCs has been described in the literature (Boujemaoui, Mongkhontreerat, Malmström, & Carlmark, 2015; Kedzior et al., 2016; Morandi et al., 2009; Zoppe et al., 2010). However, the major issues with SI-ATRP are the difficulty in characterizing grafted polymers and recovery of the free homopolymer. Control of the polymerization is generally studied using polymers obtained from a sacrificial initiator, from which the kinetics of the polymerization is considered similar to polymerization from the surface of CNCs. By recovering and characterizing the free homopolymer, information about the grafted chains can be

acquired (Hansson et al., 2011). It should be noted that this step of cleaning is challenging and crucial for characterizing both grafted CNCs and free polymers.

The aim of this study is to graft polymer brushes of various lengths at the surface of CNCs *via grafting-from* SI-ATRP. Numerous studies have focused on the polymerization of various polymers on CNCs, mostly in order to compatibilize these nanomaterials with various polymer matrices. Recently, Zoppe et al. studied the synthesis of poly(N,N-dimethylacrylamide) chains at the surface of CNCs and carried out an alkaline hydrolysis to remove and analyze the polymerized chains (Zoppe et al., 2016). Sessini et al. reported the polymerization via *grafting-from* of L-lactide and ε-caprolactone at the surface of CNCs and studied the morphological, thermal, and mechanical properties of such modified CNCs in various polymer matrices (Sessini et al., 2018).

The objective of the present study is to graft the poly(glycidyl methacrylate) (PGMA) obtained from the polymerization of glycidyl methacrylate (GMA), an epoxy-functional and commercially available monomer (Cañamero et al., 2004) on CNCs, and to produce poly(lactic acid) (PLA)-based nanocomposites. The traditional method of polymerizing GMA in a controlled manner is by atom transfer radical polymerization (ATRP), with the use of an initiator and a catalyst system (Cañamero et al., 2004). These methods aim to control the polymerization behavior. PGMA was selected for this study because of its hydrophobicity (Nyström et al., 2006) and the presence of the highly reactive epoxy functions, which can be an active attachment point for further modifications. To our knowledge, such a strategy is new in the field of CNC modification and with respect to this reactive polymer at the surface of CNCs. Control of the polymerization is essential to quantify the polymer and is conducted through SI-ATRP, as mentioned previously. To the best of our knowledge, PGMA has never been polymerized at the surface of CNCs via a *grafting-from* SI-ATRP approach. Martinez-Sanz et al. grafted PGMA via a non-controlled polymerization applied on bacterial cellulose nanowhiskers for PLA nanocomposites applications (Martínez-Sanz et al., 2013). Hansson et al. grafted various polymers, including PGMA from a cellulosic filter paper substrate, via activators regenerated by electron transfer (ARGET) ATRP to limit the use of reducing reagents and avoid the use of a totally inert atmosphere (Hansson, Östmark, Carlmark & Malmström, 2009). Malmström et al. presented different ways of functionalizing cellulose papers by controlling the surface grafting (Malmström & Carlmark, 2012) and grafted PGMA via SI-ATRP but the grafting was done at the surface of cellulose fibres to introduce a large amount of oxirane groups. More recently, Cheng et al. performed a similar

139 SI-ATRP of GMA from a nanoporous cellulose gel (NCG) followed by a hydrophobic modification of
140 polymerized NCG to produce functional materials based on NCGs (Cheng, Wei, Zhang & Cai, 2018).

141 PLA was chosen in this study as an example of a hydrophobic polymer matrix. This bio-based
142 polymer is interesting because of its biodegradability. However, to compete with the synthetic
143 polymers usually used in the packaging field, for example, the barrier and mechanical properties of
144 PLA need to be improved. This explains the many studies performed regarding the development of
145 PLA-based nanocomposites, particularly the introduction on nanocelluloses as fillers (Etzael Espino-
146 Pérez et al., 2018; Miao & Hamad, 2016; Robles et al., 2015).

147 In the present paper, an efficient SI-ATRP polymerization of GMA from the surface of CNCs is
148 described. The experiment method covers various steps. First, CNCs are functionalized with α-
149 bromoisobutyryl bromide (BIB), a brominated initiator commonly used in ATRP (Cañamero et al.,
150 2004; Morandi et al., 2009). Then, GMA is polymerized from these initiator sites, with challenges like
151 control and recovery of the homopolymer. Polymerized CNCs at different polymerization times are
152 characterized using various techniques, from bulk characterization (FTIR, elemental analysis, TGA) to
153 surface characterization (XPS). Finally, 10 wt% of the polymerized CNCs are introduced in a PLA
154 matrix, and the resulting nanocomposites are observed using microscopic technique in order to
155 investigate the compatibilization between CNCs and PLA.

156

157 **2. Materials and methods**

158 **2.1. Materials**

159 Cellulose nanocrystals (CNCs) were produced from wood pulp and purchased from CelluForce
160 (Quebec, Canada), in spray-dried form. 4-(dimethylamino)pyridine (DMAP), triethylamine (TEA), α-
161 bromoisobutyryl bromide (BIB), ethyl α-bromoisobutyrate (EBIB), and N,N,N',N'',N''-
162 pentamethyldiethylenetriamine (PMDETA) were supplied from Sigma-Aldrich Chimie (Saint-
163 Quentin-Fallavier, France) and were used as received. Copper (I) bromide (CuBr) was purchased from
164 Sigma-Aldrich Chimie. CuBr was purified by washing in glacial acetic acid for 24 h at ambient
165 temperature, filtered, rinsed extensively with ethanol and diethyl ether, dried under vacuum, and
166 stored in an inert atmosphere before use (McCaig et al., 2014). Glycidyl methacrylate (GMA) was
167 purchased from Fisher Scientific (France) and purified through a basic alumina column to remove

168 stabilizers before use. N,N-Dimethylformamide (DMF) was purchased from Sigma-Aldrich Chimie,
169 stored, and used in anhydrous conditions. Dichloromethane (DCM) and ethanol (EtOH) were
170 purchased from Sigma-Aldrich Chimie and used as received.

171 **2.2. Functionalization of CNC with α-Bromoisobutyryl Bromide**

172 Functionalization of CNC with BIB was performed by esterification reaction according to the protocol
173 adapted from Morandi et al. (Morandi et al., 2009). This protocol is as follows. First, 1.0 g of dry
174 CNCs was dispersed in 100 mL of anhydrous DMF and an ultrasonic treatment was applied. Then, 125
175 mg of DMAP (1.02 mmol) was solubilized in 2 mL of anhydrous DMF and added to the CNC
176 suspension. Thereafter, 2.1 mL of TEA (14.9 mmol) was added, followed by 1.9 mL of BIB (14.9
177 mmol). The reaction was performed at room temperature for 24 h, under argon flow. At the end of the
178 reaction, the functionalized CNC-Br were washed by successive cycles of centrifugation (9000 rpm,
179 10', 5 °C): in DMF once, in DCM twice, in a mixture of DCM/EtOH (1/1, v/v) once, and in EtOH
180 twice. CNC-Br were then dried under vacuum.

181 **2.3. SI-ATRP of Glycidyl Methacrylate on functionalized CNC-Br**

182 The method for SI-ATRP of GMA onto CNCs was adapted from classical ATRP of this monomer
183 (Cañamero et al., 2004). First, 0.5 g of previously functionalized CNC-Br was redispersed in a Schlenk
184 in 10 mL of anhydrous DMF and magnetically stirred under argon, before being treated with
185 ultrasound. Then, 0.054 mL of EBIB, 0.076 mL of PMDETA, and 4.8 mL of purified GMA were
186 successively added to the suspension ($[GMA]_0$:$[EBIB]_0$:$[PMDETA]_0$:$[CuBr]_0$ = 100:1:1:1). The
187 sacrificial EBIB was added to react as a sacrificial initiator, assuming that the polymerization of GMA
188 occurred from this initiator, in the same manner as from the surface of our CNC-Br. Next, 0.054 g of
189 CuBr was introduced quickly and at the last moment, to avoid oxidation, noticeable by a colour change.
190 A flow of argon was set up in the closed Schlenk under magnetic stirring. A total of 7 freeze-thaw
191 cycles were carried out to completely remove oxygen from the suspension. The mixture was then
192 magnetically stirred under argon at room temperature for 24 h. Study of the polymerization kinetics
193 was performed by collecting aliquots of the reaction media with a purged argon syringe. At the end of
194 the reaction, a small amount of DCM was added to recover all the mixture and a first centrifugation
195 cycle (9000 rpm, 15', 5 °C) was carried out. The supernatant containing PGMA polymerized from the
196 sacrificial initiator was recovered for characterization. The centrifuged part was further washed in
197 DCM with five cycles of centrifugation (9000 rpm, 15', 5 °C) to eliminate all the free homopolymer
198 and to only retrieve CNC-PGMA-Br. The solubilized PGMA homopolymer recovered in the DCM

199 supernatant was purified on a basic alumina column, precipitated in cold methanol, filtered, and dried
200 under vacuum.

201 **2.4. Polymerization of homopolymer PGMA**

202 The reference homopolymer PGMA was prepared by ATRP according to the previously described
203 method. Indeed, the same protocol was used without CNC and a sacrificial initiator and with
204 $[GMA]_0$:$[PMDETA]_0$:$[CuBr]_0$ = 100:1:1. After 7 freeze-thaw cycles, polymerization occurred at room
205 temperature for 1 h. At the end of the reaction, solubilized PGMA was purified on a basic alumina
206 column and precipitated in cold methanol. After filtration and drying, PGMA homopolymer was
207 characterized by ^{1}H-NMR, and a conversion rate of 52% and a theoretical molar mass of 7300 $g.mol^{-1}$
208 was calculated. This homopolymer was used as reference PGMA in this study.

209 **2.5. PLA-based nanocomposites preparation**

210 First, a 10 wt% PLA solution was prepared by dissolving PLA pellets in dichloromethane under
211 constant magnetic stirring for a whole night. Neat CNCs or polymerized CNC-PGMA-Br were solvent
212 exchanged to dichloromethane and introduced into the PLA solution. The mixture was then
213 homogenized using an Ultra-Turrax homogenizer (IKA) following by an ultrasound treatment (10
214 $kJ.g_{CNC}^{-1}$), and then poured into a Teflon petri dish. The latter was left to evaporate under a fume hood
215 for 48 h. The recovered films were then hot pressed between two Teflon sheets and with the use of a
216 150-µm-thick mould. Hot pressing was performed at 180 °C, first for 3 min without pressure, and then
217 for 1 min under 150 bar pressure. After the compression, the samples were cooled down to room
218 temperature. The films prepared with 10 wt% of neat CNCs or polymerized CNC-PGMA-Br are
219 respectively referenced as PLA_CNC10 or PLA_CNC-PGMA-Br10.

220 **2.6. Characterization methods**

221 2.6.1. Atomic Force Microscopy (AFM)

222 AFM images of CNC suspensions were recorded using a Dimension Icon Brucker equipped with a
223 silicon-coated micro cantilever (O-TESPA) using tapping mode. Droplets of diluted CNC suspension
224 (10^{-4} wt%) were deposited on clean mica plates, which were allowed to dry by evaporation overnight.
225 Approximately ten scans of 10 µm x 10 µm and 3 µm x 3 µm were obtained for each sample to
226 analyze the morphology of the nanoparticles by measuring the dimensions of at least 50 CNC samples
227 using ImageJ software.

228 2.6.2. Transmission Electron Microscopy (TEM)

229 TEM copper grids with thin amorphous carbon films were submitted to glow discharge in an easiGlow
230 station (Pelco). A 4-µL diluted CNC suspension droplet was deposited on the carbon film, followed by
231 a droplet of uranyl acetate (2 wt%). Negative dye in excess was absorbed, and the remaining film was
232 dried. The CNC suspension was observed through a transmission electron microscope FEI/Philips
233 CM200 with the microscopy NanoBio-ICMG platform (Grenoble, France), under an acceleration
234 voltage of 200 kV. Pictures were recorded with a digital camera TVIPS TemCam F216 (2040 x 2040
235 pixels). Representative images were selected for the analysis.

236 2.6.3. X-Ray Diffraction and Crystallinity Index (CI)

237 The crystallinity of CNCs was investigated with spectra obtained from wide-angle X-ray diffraction
238 analyses. An X'Pert Pro MPD diffractometer supplied by PANalytical equipped with an X' accelerator
239 detector and a copper anode (Kα (Cu) = 1.5419 Å) was used for the symmetric scan of the reflection
240 (theta/2theta in Bragg Brentano geometry) of the sample. Scans were performed from 5° to 60°. The
241 crystallinity index of samples was determined according to the Segal height peak method (Ahvenainen
242 et al., 2016; Park et al., 2010; Segal et al., 1959) (**Equation 1** below).

243 $$CI = (1 - I_{am}/I_{002}).100$$

244 **Equation 1.** Cristallinity index (CI) according to the Segal height peak method

245 where I_{am} corresponds to the intensity at the minimum (at 2θ ≃ 18.3°) and I_{002} corresponds to the main
246 crystalline peak (at 2θ ≃ 22.5°). This method is the most widely used, although it slightly
247 overestimates the value of the crystallinity and provides qualitative values of the crystallinity. The
248 measures were duplicated.

249 2.6.4. Dynamic Light Scattering (DLS)

250 The hydrodynamic diameters of CNCs were measured using a Zeta Sizer NanoZS supplied by
251 Malvern Instruments (Orsay, France), operated with DTS software. Suspensions of CNCs at 10^{-2} wt%
252 in DCM were freshly prepared before each measurement and treated in an ultrasonic bath. A total of 5
253 acquisitions with 15 measurements at 25 °C were performed and particle size average values are
254 presented. These values correspond to the diameter of the sphere diffusing at the same rate as the
255 measured particle. Moreover, the Brownian motion-induced particle speed is correlated to the size of
256 the particle by the Stokes-Einstein equation. Boluk and Danumah (Boluk & Danumah, 2014) provided
257 details of this principle applied to CNC analysis.

2.6.5. Thermogravimetric Analysis (TGA)

TGA thermograms were recorded using a thermal analyzer (NETZSCH STA 449 F3 Jupiter) from the LRMO team of the Commissariat à l'énergie atomique et aux énergies alternatives (CEA, Saclay, France). Dried samples were introduced in aluminum crucibles and were heated from 30 °C to 500 °C at 10 °C/min under helium flow at 60 mL/min. Data were at least duplicated and analyzed using Proteus software.

2.6.6. Fourier-Transform Infrared Spectroscopy (FTIR)

Infrared spectra of CNCs were performed on a Bruker IFS 66 spectrometer using an attenuated total reflectance (ATR) module composed of diamond crystals from Pike technologies. Absorbance spectra were registered between 600 and 4000 cm^{-1}, with a resolution of 4 cm^{-1} and 300 scans. Spectra were visualized and normalized using OPUS software and were at least duplicated.

2.6.7. Elemental Analysis

Elemental analyses of CNCs were performed by the "Institut des Sciences Analytiques" (Villeurbanne, France), using an ISA-CNRS micro analyzer. Based on elemental organic microanalysis, the carbon, hydrogen, oxygen and sulfur contents of the samples were determined with a precision of ±0.4% by at least duplicates. The data can be used for the determination of the degree of substitution (DS) of the grafted CNCs, equivalent to the number of functionalized hydroxyl groups per anhydroglucose unit (AGU), in accordance with **Equation 2** below (Etzael Espino-Pérez et al., 2014):

$$DS = (M(C)_{AGU} - \omega_C.(M_{AGU}+DS_{SO3}.M_{SO3})) / (\omega_C.M_{grafted} - M(C)_{grafted})$$

Equation 2. Degree of substitution (DS)

where $M(C)_{AGU}$ is the carbon molar mass of an AGU, M_{AGU} is the molar mass of an AGU, ω_C is the carbon weight fraction (in %) obtained from elemental analysis, $M_{grafted}$ is the molar mass of the grafted moieties, and $M(C)_{grafted}$ is the carbon molar mass of the grafted moieties. DS_{SO3} is the degree of substitution of sulfate half ester groups similarly calculated from the sulfur weight fraction (S%), M_{SO3} is the molar mass of $–OSO_3^-$ groups and M_S the sulfur molar mass of $–OSO_3^-$ groups, as shown in **Equation 3** below:

$$DS_{SO3} = (S\%.M_{AGU})/(M_S - \%S.M_{SO3})$$

Equation 3. Degree of substitution of half sulfate ester groups (DS_{SO3})

Taking the presence of these groups into account allows the correction of the values of carbon and oxygen weight fractions by multiplying the experimental values by $1+((DS_{SO3}.M_{SO3})/M_{AGU})$. Other

288 correction methods have also been proposed in the literature (Etzael Espino-Pérez et al., 2014;
289 Siqueira, Bras, & Dufresne, 2010).

290 2.6.8. X-Ray Photoelectron Spectroscopy (XPS)

291 XPS measurements were carried out on a K-Alpha Thermo Fisher spectrometer, equipped with a
292 monochromatic X-ray source (Al Kα, 1486.6 eV). A spot size of 400 mm was used for all
293 measurements, and a hemispherical analyzer was operated in constant analyzer energy mode with a
294 pass energy of 200 eV and a step size of 1 eV (for survey spectra) and a pass energy of 50 eV and a
295 step size of 0.1 eV (for high-resolution spectra). To neutralize the accumulation of charge, a dual-beam
296 flood gun was used. Data treatment was carried out with Avantage software (Thermo Fisher).
297 Background subtraction (Shirley type) and normalization of peak areas (using Scofield sensitivity
298 factors) were performed before any calculation of elemental composition. Binding energies are
299 referenced to the C1s neutral carbon peak at 285.4 eV.

300 2.6.9. ^{1}H-Liquid State Nuclear Magnetic Resonance (1H-NMR)

301 ^{1}H-NMR analyses were performed on a Bruker 360 MHz spectrometer in deuterated chloroform at
302 room temperature, with a residual signal appearing at 7.24 ppm. Chemical shift values were calculated
303 with TMS as the first reference. Spectra were analyzed using NMR Notebook software.

304 2.6.10. Size-Exclusion Chromatography (SEC)

305 Polymeric samples were dissolved in tetrahydrofuran (THF) at a concentration of 1 mg/mL. SEC
306 analyses were carried out with a two-column ViscoGel mixed bed from Viscotek (7.8 x 300 mm, type
307 GMHH r-H). This mixed bed was mounted on a device equipped with a refractive index detector
308 (Waters 410). The injected volume of sample solution was equal to 50 µL. The calibration range
309 corresponded to linear polystyrene standards. The process was duplicated.

310 2.6.11. Scanning Electron Microscopy (SEM)

311 Sample cross-sections of PLA_CNC10 and PLA_CNC-PGMA-Br10 were prepared by cryofracture or
312 at ambient temperature. Briefly, each sample was fractured in liquid nitrogen and was allowed to
313 return at room temperature. Fractured samples of 3 nm thickness were then metallized with
314 gold/palladium. On the other hand, 90-nm-thick sample cuts at room temperature were performed
315 using an ultra-microtome UC6 (LEICA) equipped with a diamond knife, and were then metallized as
316 previously described. For each sample, cross-sections obtained by both cryofracture or at ambient

317 temperature were analyzed using a Quanta 250 FEG (Thermofischer) device at a 2.5 kV voltage in
318 high vacuum mode. Cross-sections images were processed using ImageJ software.

319 3. Results and discussion

320 3.1. Characterization of cellulose nanomaterials

321 Commercial spray-dried cellulose nanocrystal powder was used in this study (**Figure 1 a**). These
322 CNCs are produced from wood by sulfuric acid hydrolysis of bleached pulp (Reid et al., 2016) and can
323 easily be redispersed at low concentration in water and polar organic solvents (such as DMF or
324 DMSO) using ultrasound treatment with an ultrasonic probe (Viet, Beck-Candanedo & Gray, 2007).

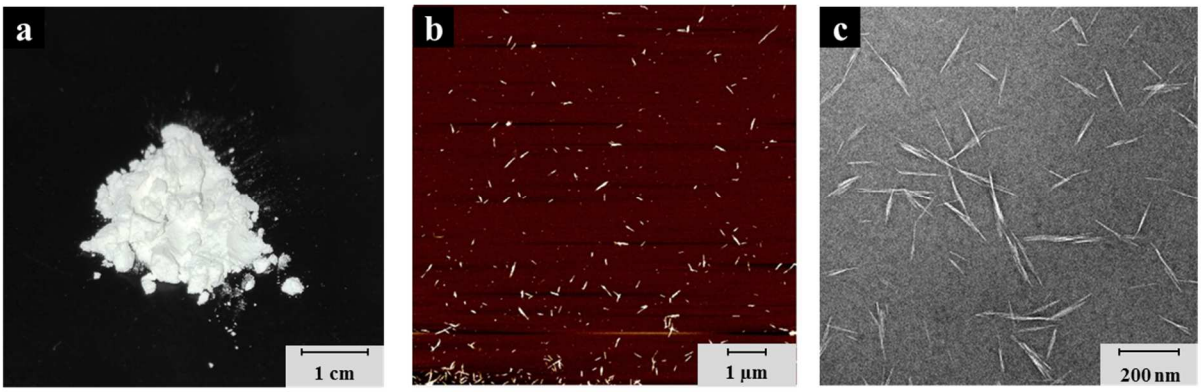

325

326 **Figure 1. a)** Spray-dried CNC from CelluForce; **b)** AFM height image of CNC and **c)** TEM image of CNC

327 Using the AFM and TEM images (**Figure 1 b and c**), morphology of the neat nanomaterials can be
328 confirmed, and the average length is 108 +/- 33 nm and average diameter is 4 +/- 1 nm, confirming the
329 values found in the literature (Foster et al., 2018; Reid et al., 2016). The X-Ray diffractograms (**Figure**
330 **2 a**) display three main peaks, at 16.2° (signal 110), 22.6° (signal 200), and 34.6° (signal 004),
331 characteristic of the cellulose I crystalline form. Moreover, the CI calculated according to **Equation 1**
332 has a value equal to 91%, consistent with the high crystallinity of CNC presented in the literature
333 (Habibi et al., 2010).

334 3.2. Preparation of initiator modified CNC

335 BIB is a common reagent used in the CNC functionalization based on ATRP. As found in the literature
336 (Boujemaoui et al., 2015; Morandi et al., 2009; Nyström et al., 2006), this grafting introduces highly
337 reactive brominated functionality at the surface of nanomaterials. These functionalized sites can then
338 be used as initiator sites for further controlled radical polymerization reactions. In the present study,
339 the brominated functionalized site at the surface of the CNC-Br served as initiators for the SI-ATRP

340 applied to the GMA monomer. The functionalization of CNCs with BIB, leading to CNC-Br, is
341 illustrated in **Scheme 1** below.

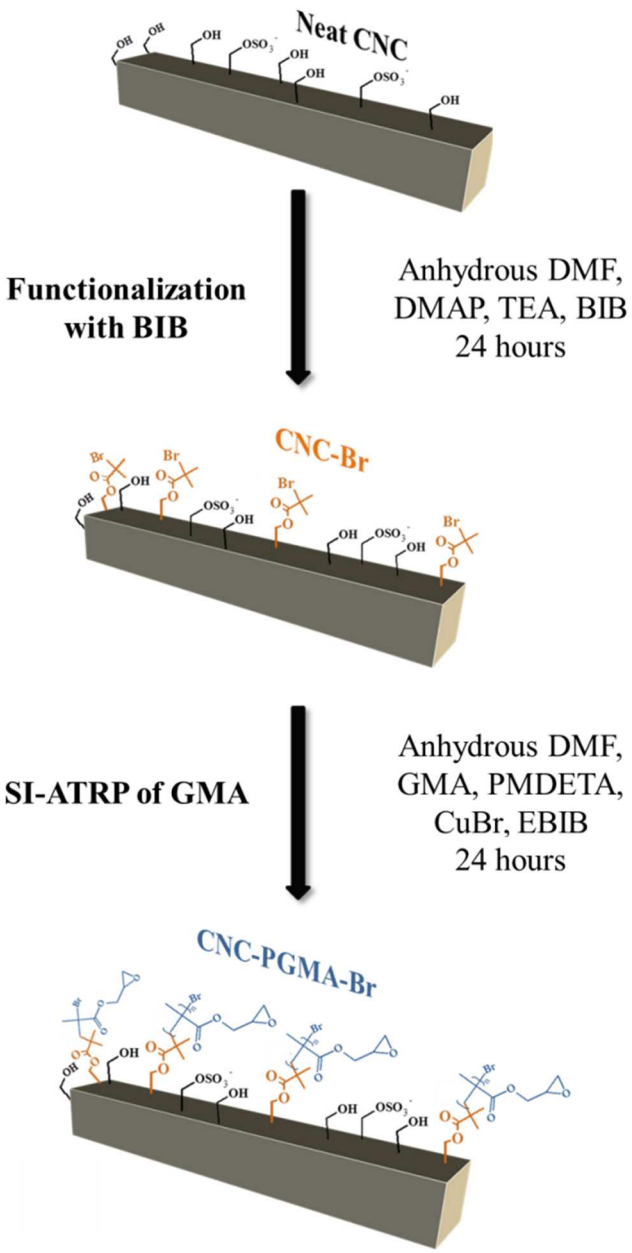

342

343 **Scheme 1.** Procedure for to the preparation of CNC-Br and CNC-PGMA-Br materials

344 Conservation of the structure of the CNCs after their functionalization is crucial and has been
345 investigated by XRD analyses. **Figure 2 a** shows wide-angle diffractogram of modified CNC-Br,
346 whose spectra correspond to cellulose I *beta*. The calculated CI is equal to 86%, confirming the
347 conservation of the crystalline structure of CNC-Br. Modified CNC-Br are well-dispersed in DCM,
348 with a mean apparent diameter size of 122 nm, which is similar to that of neat CNC dispersed in DCM
349 (**Figure 2 b**). Even if the dispersion of CNC in DCM does not lead to conclusions regarding their

dispersion in DMF, the dispersion state in DCM provides some insight about their dispersion in polar DMF. This dispersion should theoretically be greater. Thus, it is likely that isolated CNC-Br in DMF would provide a large accessible surface for further polymerization.

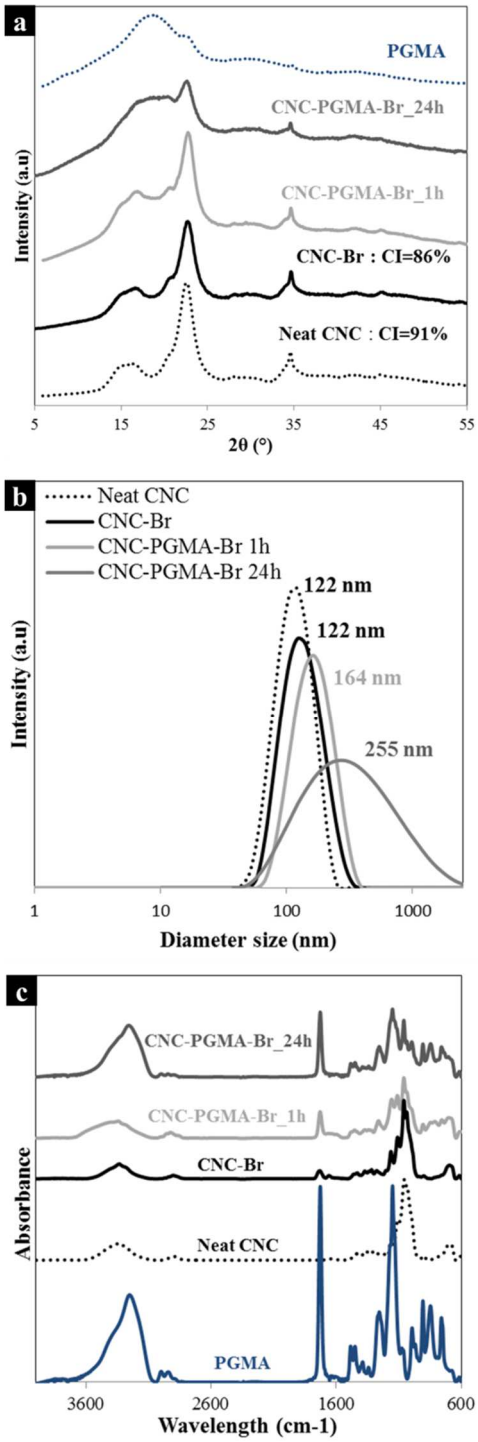

Figure 2. a) X-ray diffractograms of neat CNCs, pre-functionalized CNC-Br, CNC-PGMA-Br after 1 h and 24 h of polymerization and PGMA homopolymer; **b)** DLS curves of neat CNC, pre-functionalized CNC-Br and CNC-PGMA-Br after two different polymerization times in dichloromethane; and **c)** FTIR spectra of PGMA homopolymer, unmodified CNC, grafted CNC-Br, polymerized CNC-PGMA-Br-1h, and CNC-PGMA-Br_24h

358 FTIR analyses carried out on neat CNC and modified CNC-Br clearly show the efficiency of the
359 grafting of BIB. Indeed, in addition to the characteristic peaks of cellulose (i.e., large peak between
360 3000 cm^{-1} and 3700 cm^{-1} corresponding to the stretching vibrations bands of the -OH bonds of
361 hydroxyl groups, as well as peaks at 1110 cm^{-1}, 1060 cm^{-1} and 1035 cm^{-1} corresponding to the
362 vibration of the -C-O bonds of carbons from the repeating unit of cellulose), the peak at 1730 cm^{-1} is
363 correlates to the -C=O vibration band resulting from ester functional units introduced at the surface of
364 CNC (**Figure 2 c**).

365 Moreover, no peak near 1760-1800 cm^{-1} corresponding to the (-C=O)-Br bond from unreacted BIB is
366 observed. This confirms the efficiency of the washing steps after the reaction. Elemental analyses were
367 carried out on unmodified CNC and grafted CNC-Br to confirm this grafting (**Table 1**). Corrected
368 values were obtained by considering the presence of half-sulfate ester groups at the surface of CNCs,
369 and the DS of the grafts on the CNCs that were equal to 0.17 was calculated according to **Equation 2**.
370 Differences between the corrected values for neat CNC and theoretical values for pure cellulose can be
371 attributed to the presence of hemicelluloses and impurities in the raw materials. The calculations
372 performed in this study are based on the values corrected according to the method proposed previously
373 (**Equation 2).**

Sample	Experimental values				DS_{SO3}	Corrected values		Experimental O/C	Theoretical O/C	DS	%PGMA
	%C	%O	%H	%S		%C	%O				
Neat CNC	40.7	50.8	6.4	0.8	0.04	41.5	51.8	1.2	1.1	-	0
CNC-Br	42.0	45.3	6.0	0.8	0.04	42.8	46.2	1.1	0.8	0.17	0
CNC-PGMA-Br_1h	49.6	37.0	6.9	0.6	0.03	50.6	37.7	0.7	0.7	-	48
CNC-PGMA-Br_24h	53.2	36.7	6.9	0.2	0.01	54.2	37.4	0.7		-	70
PGMA (theoretical)	-	-	-	-	-	59.1	33.8	-	0.6	-	100

374 **Table 1.** Atomic composition of neat CNCs, CNC-Br, CNC-PGMA-Br_1h and CNC-PGMA-Br_24h obtained by elemental
375 analysis

376 To further determine and quantify the grafting at the surface of CNC-Br, XPS measurements were
377 taken allowing the characterization of the surface of the materials as being approximately 10 nm in
378 depth (Morandi et al., 2009). **Figure 3 a** shows the XPS surveys of neat CNC and grafted CNC-Br.
379 Both spectra are composed of two main peaks at approximately 534 and 288 eV corresponding to the
380 oxygen and carbon components, respectively. A peak at 71 eV correlated with a bromine component is

visible in the CNC-Br survey, and quantification of the Br3d spectrum leads to an atomic percentage of bromine equal to 1.0% at the surface of CNC-Br. **Figure 3 b and c** show the decomposition spectra of the C1s signal for both neat and grafted CNC-Br.

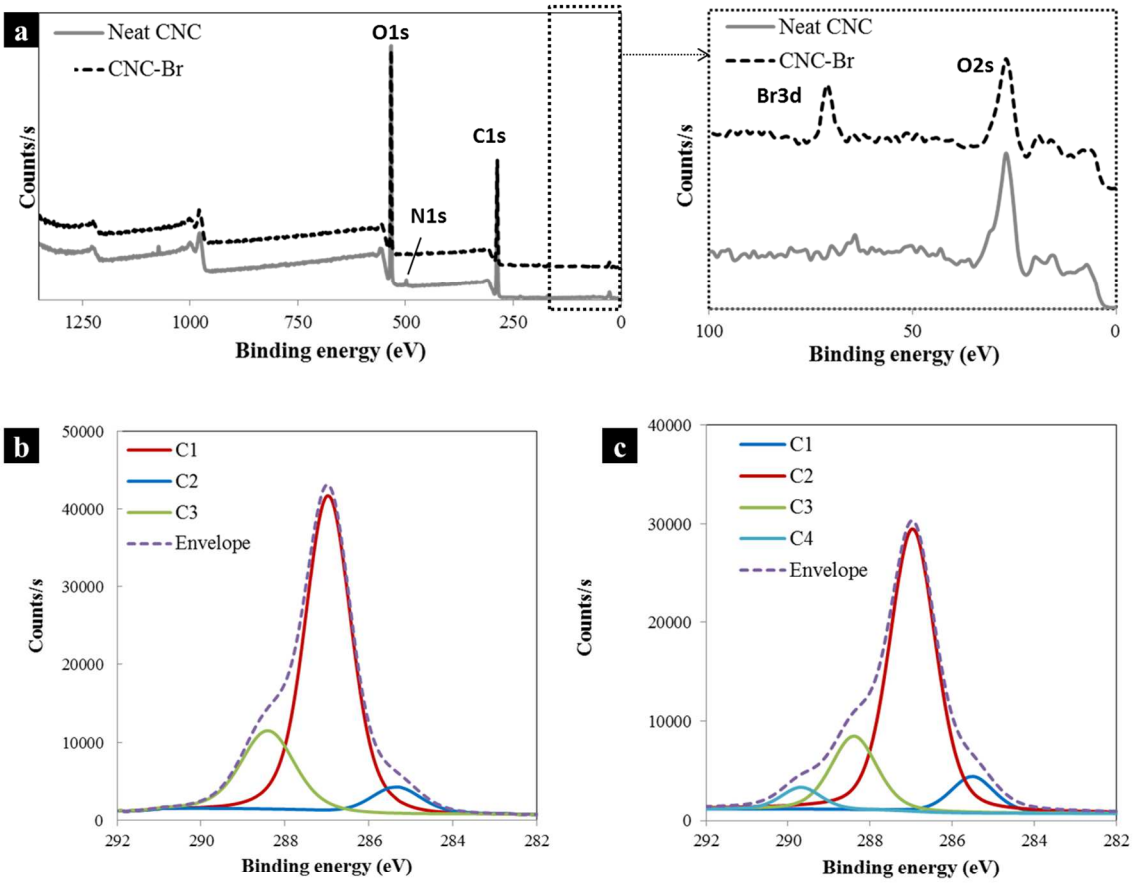

d

Sample	Experimental values			C1s decomposition					
	%C	%O	O/C	C-C / C-H	C-O	O-C-O / C=O	O-C=O	C*-C=O	C-O-C (epoxy ring)
Neat CNC	56	44	0.79	7	72	21	-	-	-
CNC-Br	57	41	0.72	8	69	18	5	-	-
CNC-PGMA-Br_1h	68	32	0.47	29	13	-	9	15	33
CNC-PGMA-Br_24h	70	30	0.43	21	17	-	16	18	28
PGMA homopolymer	72	28	0.39	30	31	-	13	13	13

Figure 3. a) XPS survey of neat CNCs and grafted CNC-Br and decomposition of the C1s peak of **b)** neat CNCs and **c)** CNC-Br spectra; and **d)** elemental molar compositions and surface functional group compositions obtained by XPS analysis

The neat CNC spectrum displays three peaks, at 285.4 eV, 287.0 eV (ΔeV= 1.6 eV), and 288.4 eV (ΔeV= 3 eV), corresponding to C1 (C-C/C-H), C2 (C-O), and C3 (O-C-O/C=O) bonds respectively. The C1 signal is present in the neat CNC spectrum but is related to the contribution of non-oxidized alkane-type carbon atoms and impurities, residual lignin, or extractive compounds, justifying its presence. The C2 signal is related to the presence of ether groups from pure cellulose, as well as the hydroxyl groups of the unmodified CNCs and of the end of the cellulose chains, explaining its

394 presence in both samples. The C3 signal corresponds to acetal moieties from AGU units and should
395 not change significantly after chemical modification, because the corresponding carbon is not affected.
396 Subsequent to α-bromoisobutyryl bromide grafting, a C4 contribution appears in the CNC-Br spectrum
397 and is correlated to the introduction of (O-C=O) bonds on the material with a ratio of 5%, which
398 confirms the success of the bromide derivative grafting, as previously described in the literature (Tian
399 et al., 2014) (**Figure 3 b)** and **d)**). In addition, the oxygen to carbon ratio (O/C) associated with the
400 sample before and after modification changed from 0.79 (close to that of pure cellulose ≈0.83
401 (Dufresne, 2018)) for the neat CNCs to 0.72 for the CNC-Br as a result of the α-bromoisobutyryl
402 bromide moiety grafted at the surface of CNCs (**Figure 3 e**). From these results, it is possible to
403 conclude the efficient grafting of CNC-Br. Thus, the presence of initiator sites for the further
404 polymerization of GMA on CNC-Br is clearly confirmed.

405 **3.3. Kinetics of the SI-ATRP of GMA**

406 Prior to any polymerization and characterization, it is essential to determine that no parallel reaction —
407 especially adsorption — occurs between cellulose and the monomer. This point was investigated by
408 applying a similar treatment to that of SI-ATRP, but without an initiator, catalyst, or ligand. Only neat
409 CNCs dispersed in anhydrous DMF in the same proportions and the GMA monomer were
410 magnetically stirred for 24 h. CNCs were then recovered after five centrifugation cycles in DCM, and
411 FTIR spectra were obtained after evaporation of the solvent (**Figure 4 a**). There is no change in the
412 FTIR spectra of neat CNC after being mixed with the monomer for 24 hours; in particular, there is no
413 peak related to a C=O bond from GMA at approximately 1720 cm^{-1}. At this stage, it can be assumed
414 that further evidence of the presence of characteristic groups of GMA and PGMA do not come from
415 possible adsorbed monomer on CNC.

416 After being grafted, CNC-Br were then polymerized at their brominated initiator sites with GMA, as
417 illustrated in **Scheme 1**. Glycidyl methacrylate (GMA) is a monomer that has never been used as part
418 of the polymerization from the surface of wood CNC, to the best of our knowledge. In the literature,
419 only a few studies describe ATRP of GMA (Barbey et al., 2013; Cañamero et al., 2004) on cellulose,
420 presented as a well-known and controlled polymerization. In our case, the difficulty of the
421 polymerization lays in the high reactivity of the epoxy groups of PGMA which can rapidly open.
422 Nevertheless, opening of these epoxy functional groups has been avoided by the reaction at room
423 temperature, in anhydrous conditions, and with the absence of any reagents that can react with these
424 groups. Moreover, it has been shown in the literature that a similar system for SI-ATRP of GMA on a

substrate (CuBr/PMDETA) leads to the conservation of active epoxy groups on the polymer chains (Wang et al., 2017). Meanwhile, the presence of these epoxy groups at the surface of polymerized CNC is one objective of this polymerization and is precisely investigated in this study. Kinetics is the key point in the understanding of a polymerization, and was investigated in this study. At different times during SI-ATRP of GMA initiated by CNC-Br materials, aliquots were withdrawn from the reaction media and analyzed by ^{1}H-liquid NMR to determine the polymerization conversion by following the disappearance of peaks related to vinyl protons from the monomer and the appearance of peaks related to protons from the methyl groups of the polymer (**Figure 4 b**).

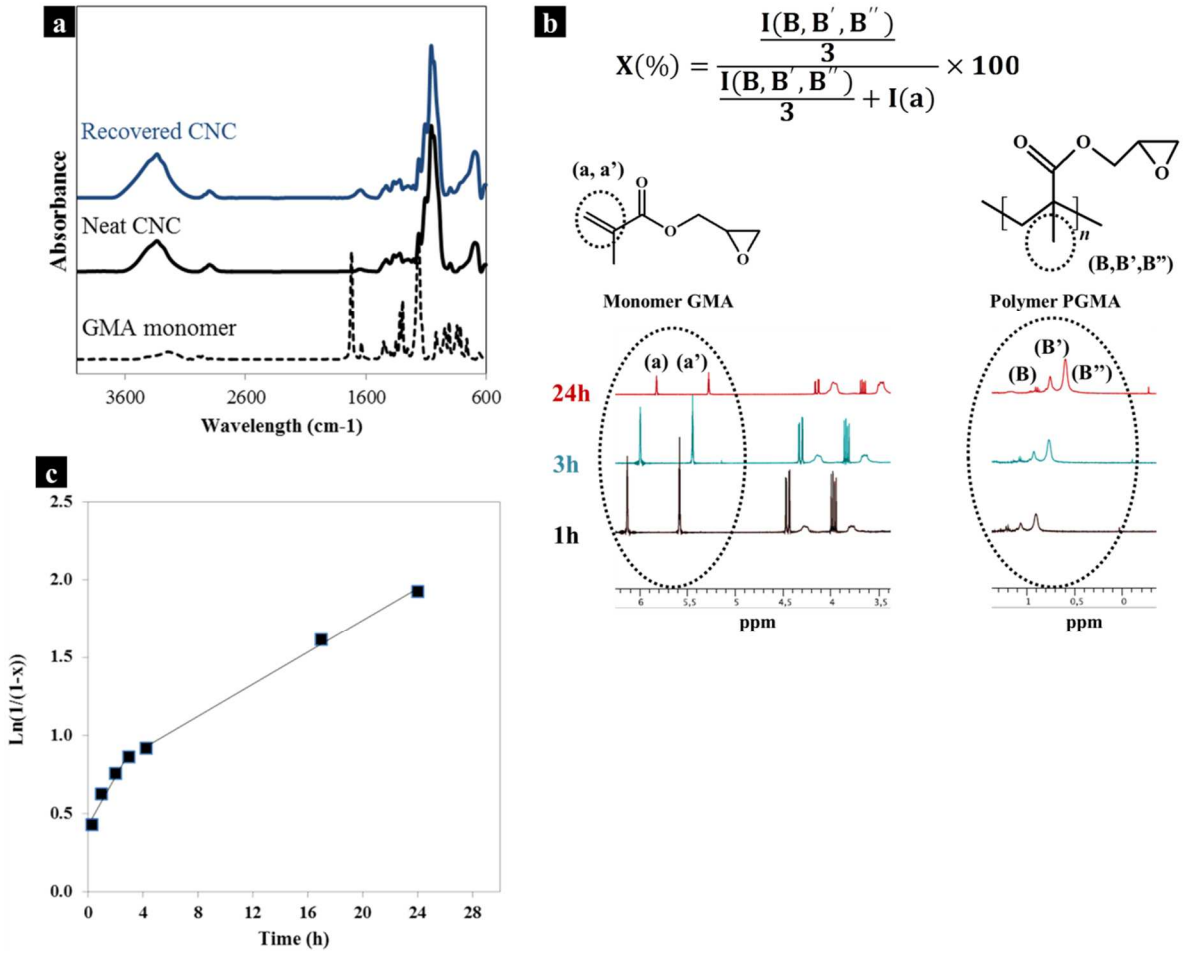

Figure 4. **a)** FTIR spectra of GMA, neat CNC and recovered CNC after mixing with GMA in conditions similar to polymerization; **b)** ^{1}H-liquid NMR spectra of the recovered reaction media after three different polymerization times, where (a) and (a') correspond to the protons of the end of the double-bond carbon-carbon of the monomer GMA and (B), (B'), and (B'') to the protons of the methyl groups of the polymer PGMA and equation of the conversion rate X calculation with I corresponding to the integral related to the area below the curve of the peak a (I(a)) or of the three peaks B, B' and B'' (I(B,B',B'')); and **c)** representation of the evolution of conversion as a function of polymerization time

The recorded NMR spectra show decreasing peak intensity at 5.6 and 6.1 ppm related to the vinyl protons of the monomer. In parallel, the intensity of the peaks between 0.9 and 1.2 ppm related to the protons from the methyl group from the growing polymer clearly increased. Conversion (p) of the

443 GMA into PGMA can be calculated using the formula presented in **Figure 4 b,** where the value I
444 corresponds to the integration of the peaks. The evolution of the conversion is represented by plotting
445 the ratio ln(1/(1-p)) as a function of time (**Figure 4 c**), showing the two rates of polymerization with a
446 higher rate in a shorter time period (between 0 and 4 h) and a slower rate after a longer polymerization
447 time period. From each collected aliquot the PGMA homopolymer was recovered after filtration on
448 basic alumina and precipitated in cold methanol. Each homopolymer sample was subjected to SEC
449 analysis to obtain the value of its molar mass (according to the equivalent polystyrene). Polydispersity
450 index Đ was calculated as the ratio of weight average molar mass (Mw) to the number average molar
451 mass (Mn). The results are presented in **Figure 5 a**.
452 The evolution of the PGMA molar masses calculated by SEC analyses as a function of the conversion
453 follows the same trend as previously mentioned with two different rates of polymerization. Indeed, in
454 the first 3 h of polymerization, the molar masses increased from 8179 $g.mol^{-1}$ to 9791 $g.mol^{-1}$,
455 followed by a slower rate of polymerization reaching molar masses equal to 10343 $g.mol^{-1}$ after 24 h
456 of reaction (**Figure 5 d**). This behavior has been previously described for a similar system
457 (GMA/CuBr/PMDETA) in the literature (Xiao et al., 2011), where it was attributed to the
458 heterogeneous character of the system inducing side-reactions at high conversion rates. Indeed, radical
459 bromine elements from the cellulose surface could be lost, inducing termination at the level of the
460 CNCs. Nevertheless, polymerization would continue in the system solution. **Figure 5 b** shows the
461 FTIR spectra of CNC-PGMA-Br at different polymerization times, recovered from the aliquots after
462 centrifugation in DCM. Qualitative analysis of these spectra confirms the polymerization on CNCs,
463 with an increase in the peak at 1725 cm^{-1} related to the C=O stretching of ester groups and the
464 presence of a peak at 910 cm^{-1} related to the C-O stretching from epoxy groups. It is interesting to note
465 that ATRP polymerization applied on the GMA monomer, involving the present CuBr/PMEDETA
466 catalytic system, ensures the preparation of an epoxy functional polymer. In fact, as shown in the the
467 literature (Sabatini, 2007), decribing the grafting of multiwalled carbon nanotubes with PGMA
468 polymer using the same ATRP polymerization procedure, a further post modification to introduce
469 molecules of interest is possible by taking advantage of the epoxy functional groups.

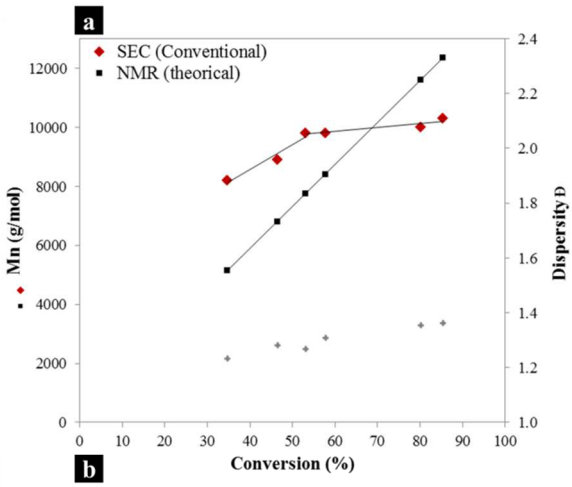

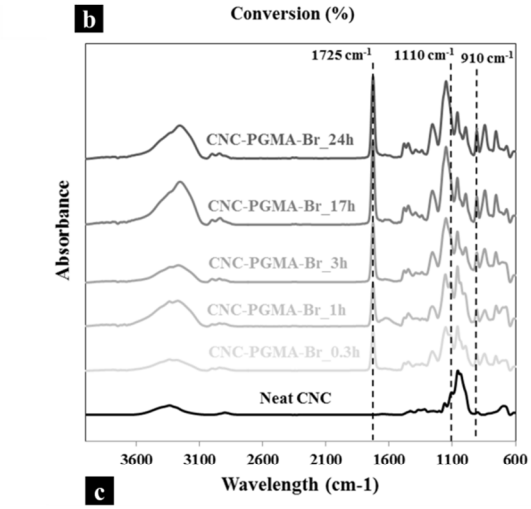

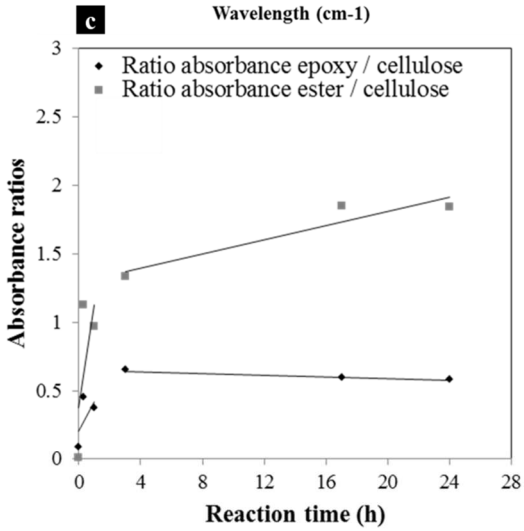

d

Time (h)	^{1}H-liquid NMR		Sec (Conventional)		FTIR absorbance ratio	
	Conversion (%)	$Mn_{theoretical}$ (g.mol^{-1})	Mn (g.mol^{-1})	Dispersity (Đ)	**Epoxy** (intensity at 910 cm^{-1}) / **Cellulose** (intensity at 1110 cm^{-1})	**Ester** (intensity at 1725 cm^{-1}) / **Cellulose** (intensity at 1110 cm^{-1})
0	0	4944	/	/	0.08	0
0.3	35	6660	8200	1.2	0.45	1.13
1	46	7552	8900	1.3	0.37	1.0
2	53	8209	9800	1.3	0.65	1.33
3	58	8529	9800	1.3	0.54	1.60
17	80	11391	10000	1.4	0.59	1.85
24	85	12145	10300	1.4	0.58	1.84

470

Figure 5. a) Molar masses of homopolymer and dispersities obtained by conventional SEC analyses; **b)** FTIR spectra of recovered CNC-PGMA-Br at different polymerization times; **c)** ratios of peak intensities related to epoxy groups/cellulose and ester groups/cellulose; and **d)** summary of kinetics study data obtained from ^{1}H-liquid NMR, SEC (conventional), and FTIR (* $Mn_{theoretical} = (p*([GMA]/[EBIB])*M_{GMA})+M_{EBIB}$ with p the conversion, [GMA] the initial concentration in monomer, [EBIB] the initial concentration in initiator, M_{GMA} the molar mass of GMA and M_{EBIB} the molar mass of EBIB (the calculation takes into account the polymer chain extremities))

Furthermore, to quantitatively analyze these spectra, the ratios of the absorbance values of both C=O and C-O peaks and cellulose (1110 cm^{-1}) were plotted as a function of time. The obtained curves (**Figure 5 c**) follow the previously mentioned trend: with short polymerization time (1 to 3 h), there is an increase in the polymer chain length at the surface of cellulose, which becomes slower at longer times (4 to 24 h). Taking into account these results (summarized on **Figure 5 d**), one hypothesis might be that the decreasing polymerization rate is due to the deactivation of brominated active sites grafted at the surface of CNC as well as those from the sacrificial initiator. A transfer reaction resulting from the hydroxyl -OH groups of CNC could be an explanation for this deactivation. In the remainder of this study, we will focus on the characterization of CNC-PGMA-Br polymerized at two different polymerization times (1 h and 24 h): CNC-PGMA-Br_1h and CNC-PGMA-Br_24h, respectively.

3.4. SI-ATRP of functionalized CNC-Br at different polymerization times

CNC-PGMA-Br_1h and CNC-PGMA-Br_24h were polymerized in larger batches for characterization, according to the previously detailed protocol. *Grafting-from* of polymers at the surface of CNCs is a widely studied procedure that allows the grafting of a high density of polymer at the surface of CNCs. In the case of the PGMA grafted as an amorphous polymer, the morphology of the final materials was investigated. **Figure 2 a** shows X-ray diffractograms of CNC-PGMA-Br_1h, CNC-PGMA-Br_24h, and PGMA homopolymer, which is not crystallized and whose XRD signature corresponds to consecutive large humps. The CNC-PGMA-Br_1h diffractogram is a combination of diffractograms of PGMA and cellulose I *beta*, with the presence of characteristic peaks at 22.6° and 34.6°. Similar to CNC-PGMA-Br_1h, CNC-PGMA-Br_24h diffractogram shows characteristic peaks of cellulose I *beta*, but the presence of the amorphous PGMA polymer is more highlighted here. These results confirm the growth of the PGMA on CNCs with increasing polymerization time.

Moreover, according to **Figure 2 b**, the diameter of polymerized CNC-PGMA-Br in DCM increases with the polymerization duration. Indeed, after 1 h, apparent diameter size is equal to 164 nm (122 nm for neat CNC and functionalized CNC-Br), which is reasonable for dispersed CNC suspension. Nevertheless, after 24 h, CNC-PGMA-Br_24h show a higher mean apparent diameter equal to 255 nm

503 and a larger peak, leading to a worse dispersion of grafted nanoparticles in the suspension. Inter-
504 particle coupling reactions between CNC-PGMA-Br is a possible explanation.

The thermal properties of polymerized CNC were investigated through TGA analyses, whose thermograms and derivative thermogravimetry (DTG) curves are presented in **Figure 6 a**, showing that polymerization of PGMA at the surface of CNC enhances the thermal stability of the materials. Indeed, the primary onset of the degradation temperature of CNCs before and after 1 and 24 h of polymerization increases from 305 °C to 314 °C and 326 °C respectively. Moreover, the CNC thermogram shows one weight loss peak between 250 °C and 350 °C. In a recent study, Zhang et al. studied different ways to characterize grafted polymers on CNCs, including the use of TGA analysis (Zhang et al., 2018). Their method appears to be not totally applicable in our case because of the presence of a weight loss peak of PGMA in the same temperature ranges as for cellulose. Moreover, the presence of a second weight loss peak for PGMA, polymerized CNC-PGMA-Br_1h, and CNC-PGMA-Br_24h between 350 °C and 480 °C allows an approximation of the amount of PGMA polymerized on CNC. Indeed, taking into account the slight weight loss of cellulose in this second temperature range for calculation, and considering that samples are only composed of cellulose and polymer, a weight percentage of PGMA equal to 38% and 83% respectively for CNC-PGMA-Br_1h and CNC-PGMA-Br_24h are calculated (**Figure 6 b**). The large amount of grafted polymer after 24 h of polymerization is confirmed. Moreover, even after a short polymerization time, nearly 40% by mass of the sample is PGMA, corresponding to the previous kinetic study of this polymerization.

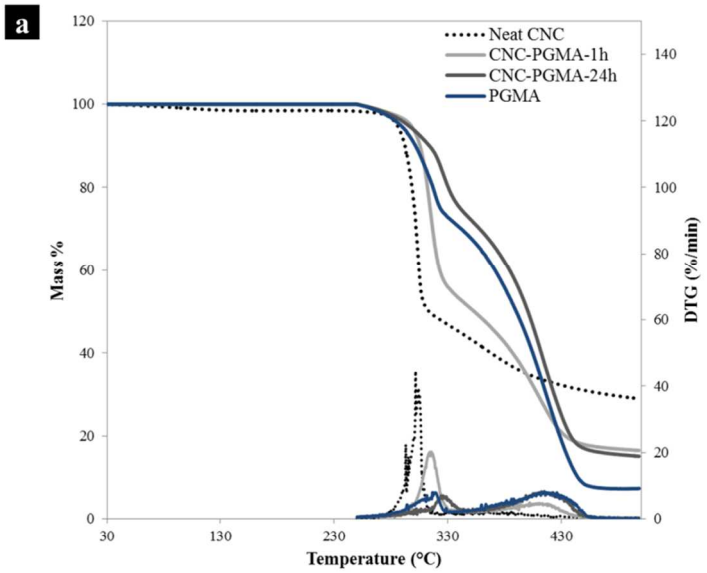

b

Sample	% weight loss (350°C-480°C)	Thermal degradation onset T_{onset} (°C)	PGMA (%wt)
CNC	14	305	0
CNC-PGMA-Br_1h	30	314	38
CNC-PGMA-Br_24h	49	326	83
PGMA homopolymer	56	319	100

Figure 6. a) TGA thermograms and DTG curves of neat CNC, CNC-PGMA-Br_1h, CNC-PGMA-Br_24h, and homopolymer PGMA; and **b)** thermal degradation onset temperatures and calculated amount of PGMA in both CNC-PGMA-Br_1h and CNC-PGMA-Br_24h

By regarding only the morphology of polymerized CNC-PGMA-Br, 1 h of polymerization ensures the conservation of the crystallinity, which is critical for further applications, while introducing a significant amount of PGMA.

3.5. Efficiency of SI-ATRP on CNCs

The efficiency of the polymerization of GMA from brominated initiator sites previously grafted on CNC was first investigated by FTIR analysis, whose spectra are shown in **Figure 2 c.** Results confirm the conclusion drawn from **Figure 5 b**, proving the efficiency of the polymerization and the growth of the polymer over time. Indeed, peaks at 910 cm^{-1}, 906 cm^{-1}, 1728 cm^{-1}, and between 2840 cm^{-1} and 3000 cm^{-1} are respectively characteristic of the epoxy groups, terminal vinyl groups and ester bonds from carbonyl groups, and $-CH_2$ and $-CH_3$ carbons from the PGMA backbone polymer. The clear increase in those peaks for the CNC-PGMA-Br_1h and CNC-PGMA-Br_24h spectra demonstrates the polymerization of PGMA at the level of CNCs over time. These results are confirmed by elemental analyses (**Table 1**). Indeed, for both CNC-PGMA-Br_1h and CNC-PGMA-Br_24h, an increase in the %C values and a decrease in the %O values are notable and consistent with the introduction of the polymer PGMA $(C_7H_{10}O_3)_n$ on CNCs. This is reaffirmed by the decrease in the O/C ratio for these polymerized CNCs, which is also similar to the corresponding theoretical calculated ratio and to those of pure PGMA. The slight difference between the O/C ratios of CNC-PGMA-Br and PGMA confirms the presence of cellulose in the sample. Note that values are corrected according to the previously described method by considering the presence of half-sulfate ester groups at the surface of CNCs, without however considering the presence of impurities like hemicelluloses in the samples, which could influence the values, so they must be interpreted comparatively. Moreover, considering that CNC-PGMA-Br_1h and CNC-PGMA-Br_24h are composed of cellulose and PGMA, an estimation of the weight percentage of PGMA may also be calculated in both cases, as presented in **Table 1**. Values are not totally equal to those previously calculated through TGA thermograms (**Figure 6 b**), but the trend is similar, keeping in mind that TGA and elemental analysis have different sensitivities and involve different approaches. The amount of PGMA with increasing polymerization time, and approximately 48% and 70% by mass of PGMA is attached to CNCs after 1 h and 24 h respectively.

One of the primary challenges to SI-ATRP on CNCs involves the characterization and quantification of the grafted polymer at the surface of the nanomaterials. Hansson at al. (Hansson et al., 2011)

555 investigated this point by proving that the kinetics of the polymerization at the surface of CNCs is
556 similar to those in the media from a sacrificial initiator. Previous characterizations allow the proof of
557 the polymerization as well as an estimate of the calculated amount of polymer. The surfaces of
558 polymerized CNC-PGMA-Br_1h and CNC-PGMA-Br_24h were investigated by XPS analyses; the
559 decompositions spectra of the C1s signal are presented in **Figure 7 c** and **d**.

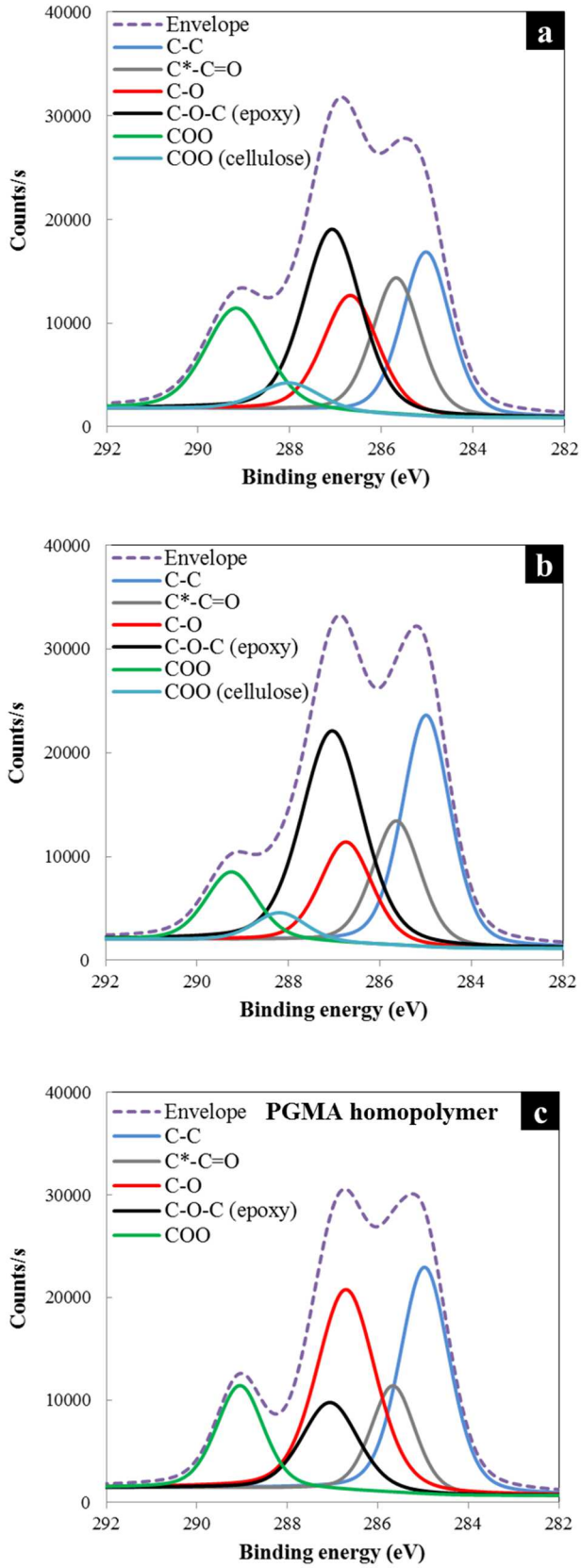

Figure 7. Decomposition of the C1s peak of **a)** CNC-PGMA-Br_1h, **b)** CNC-PGMA-Br_24h, and **c)** PGMA homopolymer obtained by XPS analyses

In **Figure 7 b**, the decomposition spectra of the C1s peak of PGMA homopolymer shows the presence of characteristic peaks of the polymer: at 285.4 eV, 286.1 eV (ΔeV = 0.7 eV), 287.1 eV (ΔeV = 1.7

565 eV), 287.5 eV (ΔeV = 2.1 eV), and 289.5 eV (ΔeV = 4.1 eV) for respectively the C-C/C-H, C*-C=O- ,
566 C-O, C-O-C (epoxy ring), and O-C=O bonds. The CNC-PGMA-Br_1h and CNC-PGMA-Br_24h
567 (**Figure 7 c** and **d**) decomposition spectra show the same characteristics, as well as a peak
568 characteristic of cellulose at 288.2 eV (ΔeV = 3.3 eV) related to the C3 signal (O-C-O or C=O) from
569 the neat CNCs. It is important to note that the intense C2 signal from cellulose is also present but is
570 superimposed over other C-O and C-O-C peaks. This result confirms the grafting of a PGMA polymer
571 layer onto CNCs.
572 Moreover, the determination of the O/C ratio (**Figure 3 e**) leads to a value of 0.47 for CNC-PGMA-
573 Br_1h materials, whereas a ratio of 0.42 is observed for CNC-PGMA-Br_24h, which is similar to the
574 theoretical value associated with pure PGMA polymer (Beamson & Briggs, 1993 reference). This
575 result could explain the increasing grafted polymer weight with time, as shown in **Figure 5 d**.
576 According to the XPS results, it is possible to make a conclusion about the presence of PGMA over
577 the surface of CNC. Moreover, it is possible to observe in **Figure 7** that after 1 h of polymerization,
578 the intensity of the peak associated with the epoxy C-O-C bond is less intense than that of the
579 homopolymer reference. After 24 h of polymerization, this intensity is closer to that of the
580 homopolymer, confirming that the amount of polymerized PGMA is more important. Quantification of
581 the polymer is not possible considering these results, but the presence of PGMA at the surface of
582 CNCs is clearly highlighted. Moreover, highly reactive epoxy rings are conserved during the
583 polymerization and are available at the surface of both CNC-PGMA-Br_1h and CNC-PGMA-Br_24h.

584 **3.6. PLA-based nanocomposites**

585 To investigate the effect of PGMA on the surface of CNCs on their compatibilization with a
586 hydrophobic polymeric system — and especially with PLA — cross-sections of PLA_CNC10 and
587 PLA_CNC-PGMA-Br10 nanocomposites were observed by SEM. Related images are presented in
588 **Figure 8**. **Figure 8 a** and **b** were obtained from cross-sections prepared respectively without and with
589 cryofracture. In **Figure 8 a**, large micrometric aggregates can be observed. Moreover, sedimentation of
590 these aggregates can be noted and may be related to the casting method used for nanocomposite films
591 preparation. **Figure 8 b** allows the observation of very distinguishable CNC aggregates. Moreover,
592 cavities are visible and demonstrate the lack of adhesion between the micrometric fillers and the
593 polymeric matrix.

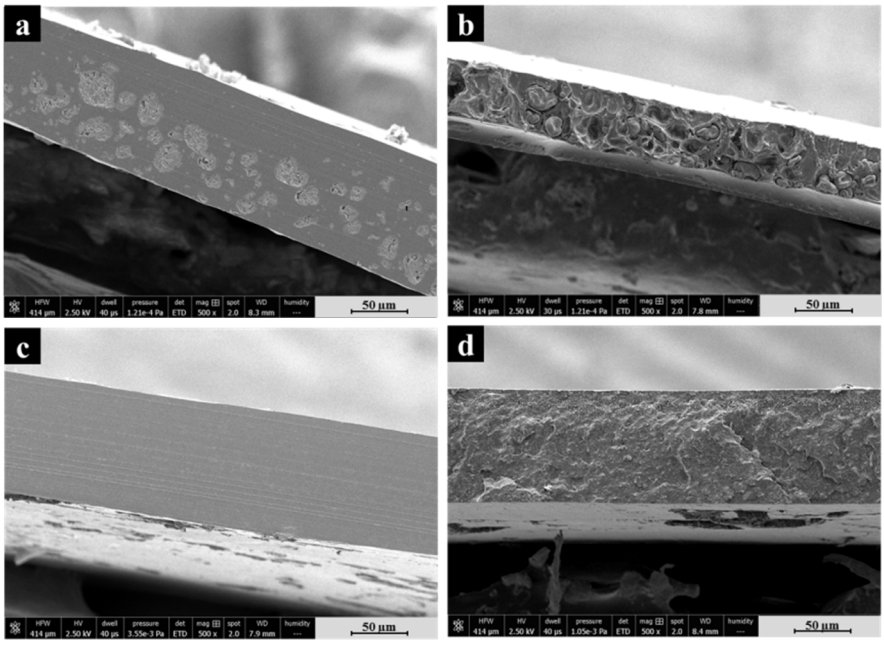

Figure 8. SEM images of cross-sections of PLA_CNC10 nanocomposite film a) without and b) with cryofracture and of PLA_CNC-PGMA-Br10 nanocomposite film c) without and d) with cryofracture

Figure 8 c and **d** show SEM images of PLA-based nanocomposites prepared with modified CNC-PGMA-Br after 1 h of polymerization. The cross-section prepared without cryofracture (**Figure 8 c**) presents a homogeneous surface. Indeed, no micrometric aggregates are visible. Moreover, the cryofractured sample (**Figure 8 d**) also exhibits a homogeneous cross-section, as no micrometric particles or cavities are visible. This result emphasizes the enhancement of the filler dispersion in the matrix, and thus the improvement of the adhesion between cellulosic nanofillers CNC-PGMA-Br and the PLA matrix. The interface between CNC-PGMA-Br and PLA is therefore improved and is the key point in the elaboration of nanocomposites, because of its influence on the physico-chemical properties of final materials.

4. Conclusion

CNCs were initially modified with BIB as an initiator of SI-ATRP of PGMA; the efficiency of the functionalization was highlighted using bulk and surface characterization. After ensuring that only the polymerized monomer is present at the level of CNCs after washing, polymerized CNC at two different polymerization times were recovered and characterized using FTIR, XRD, TGA, XPS and elemental analysis. After only 1 h of polymerization, PGMA covers almost all the surface of CNCs, with a weight percentage of approximately 40% relative to CNC. After 24 h of polymerization, the weight proportion of PGMA represents almost 80% of the total weight, but the obtained polymerized

614 CNCs are more aggregated in non-polar solvent. In both cases, the presence of characteristic bonds of
615 the polymer, and especially carbonyl groups and epoxy rings are highlighted, although 1 h of
616 polymerization seems to optimize the reaction conditions for the preparation of well-dispersed,
617 polymerized, hydrophobized CNCs for further incorporation in hydrophobic polymer matrices or
618 further chemical modification. SEM images of PLA_CNC-PGMA-Br10 nanocomposites highlight the
619 improvement of the adhesion between the polymer and the cellulosic nanofillers. Currently, this issue
620 remains the main challenge in nanocomposite field. The results presented in this study are encouraging
621 and could lead to the improvement of the barrier and mechanical properties of PLA-based materials.

622 **Acknowledgements**

623 This work was supported by the French National Research Agency (ANR) as part of the program
624 ANR-16-CE08-0040. LGP2 is part of the LabEx Tec 21 (Investissements d'Avenir – grant agreement
625 n° ANR-11-LABX-0030), of PolyNat Carnot Institute (Investissements d'Avenir – grant agreement n°
626 ANR-16-CARN-0025-01) and of CDP Glyco@Alps (ANR-15-IDEX-02). This research was made
627 possible by the facilities of the TekLiCell platform, funded by the Région Rhône-Alpes (ERDF:
628 European regional development fund). The authors would like to thank Ludovic Costa from ICMMO
629 (Orsay, France), Thierry Encinas from CMTC (Grenoble, France) and Jean-Luc Putaux and Christine
630 Lancelon-Pin from Cermav (Grenoble, France) for SEC, XRD and SEM analyses, respectively.

631 **References**

632 Abitbol, T. (2014). Surface modification of cellulose nanocrystals with cetyltrimethylammonium
633 bromide. *Nordic Pulp and Paper Research Journal*, *29*, 046-057.

634 Ahvenainen, P., Kontro, I., & Svedström, K. (2016). Comparison of sample crystallinity determination
635 methods by X-ray diffraction for challenging cellulose I materials. *Cellulose*, *23*, 1073-1086.

636 Azzam, F., Heux, L., Putaux, J.-L., & Jean, B. (2010). Preparation By Grafting Onto, Characterization,
637 and Properties of Thermally Responsive Polymer-Decorated Cellulose Nanocrystals.
638 *Biomacromolecules*, *11*, 3652-3659.

Barbey, R., Laporte, V., Alnabulsi, S., & Klok, H.-A. (2013). Postpolymerization Modification of Poly(glycidyl methacrylate) Brushes : An XPS Depth-Profiling Study. *Macromolecules*, *46*, 6151-6158.

Beamson, G., & Briggs, D. (1993). High Resolution XPS of Organic Polymers : The Scienta ESCA300 Database. *Journal of Chemical Education*, *70*, A25.

Beck, S., Méthot, M., & Bouchard, J. (2015). General procedure for determining cellulose nanocrystal sulfate half-ester content by conductometric titration. *Cellulose*, *22*, 101-116.

Belgacem, M. N. (2008). *Monomers, polymers and composites from renewable resources*. Amsterdam: Elsevier.

Boluk, Y., & Danumah, C. (2014). Analysis of cellulose nanocrystal rod lengths by dynamic light scattering and electron microscopy. *Journal of Nanoparticle Research*, *16*, 2174.

Boujemaoui, A., Cobo Sanchez, C., Engström, J., Bruce, C., Fogelström, L., Carlmark, A., & Malmström, E. (2017). Polycaprolactone Nanocomposites Reinforced with Cellulose Nanocrystals Surface-Modified via Covalent Grafting or Physisorption : A Comparative Study. *ACS Applied Materials & Interfaces*, *9*, 35305-35318.

Boujemaoui, A., Mongkhontreerat, S., Malmström, E., & Carlmark, A. (2015). Preparation and characterization of functionalized cellulose nanocrystals. *Carbohydrate Polymers*, *115*, 457-464.

Cañamero, P. F., de la Fuente, J. L., Madruga, E. L., & Fernández-García, M. (2004). Atom Transfer Radical Polymerization of Glycidyl Methacrylate : A Functional Monomer. *Macromolecular Chemistry and Physics*, *205*, 2221-2228.

Cheng, D., Wei, P., Zhang, L., & Cai, J. (2018). Surface-initiated atom transfer radical polymerization grafting from nanoporous cellulose gels to create hydrophobic nanocomposites. *RSC Advances*, *8*, 27045-27053.

663 de Castro, D. O., Bras, J., Gandini, A., & Belgacem, N. (2016). Surface grafting of cellulose
664 nanocrystals with natural antimicrobial rosin mixture using a green process. *Carbohydrate*
665 *Polymers*, *137*, 1-8.

666 Domingues, R. M. A., Gomes, M. E., & Reis, R. L. (2014). The Potential of Cellulose Nanocrystals in
667 Tissue Engineering Strategies. *Biomacromolecules*, *15*, 2327-2346.

668 Dufresne, A. (2018). *Nanocellulose : From nature to high performance tailored materials* (2. edition).
669 Berlin Boston: de Gruyter.

670 Espino-Pérez, E., Gilbert, R. G., Domenek, S., Brochier-Salon, M. C., Belgacem, M. N., & Bras, J.
671 (2016). Nanocomposites with functionalised polysaccharide nanocrystals through aqueous free
672 radical polymerisation promoted by ozonolysis. *Carbohydrate Polymers*, *135*, 256-266.

673 Espino-Pérez, Etzael, Bras, J., Almeida, G., Plessis, C., Belgacem, N., Perré, P., & Domenek, S.
674 (2018). Designed cellulose nanocrystal surface properties for improving barrier properties in
675 polylactide nanocomposites. *Carbohydrate Polymers*, *183*, 267-277.

676 Espino-Pérez, Etzael, Domenek, S., Belgacem, N., Sillard, C., & Bras, J. (2014). Green Process for
677 Chemical Functionalization of Nanocellulose with Carboxylic Acids. *Biomacromolecules*, *15*,
678 4551-4560.

679 Eyley, S., & Thielemans, W. (2014). Surface modification of cellulose nanocrystals. *Nanoscale*, *6*,
680 7764-7779.

681 Ferreira, F. V., Pinheiro, I. F., Gouveia, R. F., Thim, G. P., & Lona, L. M. F. (2017). Functionalized
682 cellulose nanocrystals as reinforcement in biodegradable polymer nanocomposites. *Polymer*
683 *Composites*, *39*, E9-E29.

684 Ferrer, A., Pal, L., & Hubbe, M. (2017). Nanocellulose in packaging : Advances in barrier layer
685 technologies. *Industrial Crops and Products*, *95*, 574-582.

686 Foster, E. J., Moon, R. J., Agarwal, U. P., Bortner, M. J., Bras, J., Camarero-Espinosa, S., Chan, K. J.,
687 Clift, M. J. D., Cranston, E. D., Eichhorn, S. J., Fox, D. M., Hamad, W. Y., Heux, L., Jean, B.,
688 Korey, M., Nieh, W., Ong, K. J., Reid, M. S., Renneckar, S., … Youngblood, J. (2018).
689 Current characterization methods for cellulose nanomaterials. *Chemical Society Reviews*, *47*,
690 2609-2679.

691 Goffin, A.-L., Raquez, J.-M., Duquesne, E., Siqueira, G., Habibi, Y., Dufresne, A., & Dubois, P.
692 (2011). From Interfacial Ring-Opening Polymerization to Melt Processing of Cellulose
693 Nanowhisker-Filled Polylactide-Based Nanocomposites. *Biomacromolecules*, *12*, 2456-2465.

694 Habibi, Y. (2014). Key advances in the chemical modification of nanocelluloses. *Chem. Soc. Rev.*, *43*,
695 1519-1542.

696 Habibi, Y., Goffin, A.-L., Schiltz, N., Duquesne, E., Dubois, P., & Dufresne, A. (2008).
697 Bionanocomposites based on poly(ε-caprolactone)-grafted cellulose nanocrystals by ring-
698 opening polymerization. *Journal of Materials Chemistry*, *18*, 5002-5010.

699 Habibi, Y., Lucia, L. A., & Rojas, O. J. (2010). Cellulose Nanocrystals : Chemistry, Self-Assembly,
700 and Applications. *Chemical Reviews*, *110*, 3479-3500.

701 Hansson, S., Antoni, P., Bergenudd, H., & Malmström, E. (2011). Selective cleavage of polymer grafts
702 from solid surfaces : Assessment of initiator content and polymer characteristics. *Polymer*
703 *Chemistry*, *2*, 556-558.

704 Hansson, S., Östmark, E., Carlmark, A., & Malmström, E. (2009). ARGET ATRP for Versatile
705 Grafting of Cellulose Using Various Monomers. *ACS Applied Materials & Interfaces*, *1*, 2651
706 -2659.

707 Hubbe, M. A., Ferrer, A., Tyagi, P., Yin, Y., Salas, C., Pal, L., & Rojas, O. J. (2017). Nanocellulose in
708 Thin Films, Coatings, and Plies for Packaging Applications : A Review. *BioResources*, *12*,
709 2143-2233.

Jorfi, M., & Foster, E. J. (2015). Recent advances in nanocellulose for biomedical applications. *Journal of Applied Polymer Science*, *132*, 41719-41738.

Kargarzadeh, H., Mariano, M., Gopakumar, D., Ahmad, I., Thomas, S., Dufresne, A., Huang, J., & Lin, N. (2018). Advances in cellulose nanomaterials. *Cellulose*, *25*, 2151-2189.

Kedzior, S. A., Graham, L., Moorlag, C., Dooley, B. M., & Cranston, E. D. (2016). Poly(methyl methacrylate)-grafted cellulose nanocrystals : One-step synthesis, nanocomposite preparation, and characterization. *The Canadian Journal of Chemical Engineering*, *94*, 811-822.

Kedzior, S. A., Marway, H. S., & Cranston, E. D. (2017). Tailoring Cellulose Nanocrystal and Surfactant Behavior in Miniemulsion Polymerization. *Macromolecules*, *50*, 2645-2655.

Klemm, D., Kramer, F., Moritz, S., Lindström, T., Ankerfors, M., Gray, D., & Dorris, A. (2011). Nanocelluloses : A New Family of Nature-Based Materials. *Angewandte Chemie International Edition*, *50*, 5438-5466.

Kloser, E., & Gray, D. G. (2010). Surface Grafting of Cellulose Nanocrystals with Poly(ethylene oxide) in Aqueous Media. *Langmuir*, *26*, 13450-13456.

Lin, N., & Dufresne, A. (2014). Nanocellulose in biomedicine : Current status and future prospect. *European Polymer Journal*, *59*, 302-325.

Lin, N., Huang, J., & Dufresne, A. (2012). Preparation, properties and applications of polysaccharide nanocrystals in advanced functional nanomaterials : A review. *Nanoscale*, *4*, 3274-3294.

Malmström, E., & Carlmark, A. (2012). Controlled grafting of cellulose fibres – an outlook beyond paper and cardboard. *Polymer Chemistry*, *3*, 1702-1713.

Martínez-Sanz, M., Abdelwahab, M. A., Lopez-Rubio, A., Lagaron, J. M., Chiellini, E., Williams, T. G., Wood, D. F., Orts, W. J., & Imam, S. H. (2013). Incorporation of poly(glycidylmethacrylate) grafted bacterial cellulose nanowhiskers in poly(lactic acid)

nanocomposites : Improved barrier and mechanical properties. *European Polymer Journal*, *49*, 2062-2072.

McCaig, H. C., Myers, E., Lewis, N. S., & Roukes, M. L. (2014). Vapor Sensing Characteristics of Nanoelectromechanical Chemical Sensors Functionalized Using Surface-Initiated Polymerization. *Nano Letters*, *14*, 3728-3732.

Miao, C., & Hamad, W. Y. (2016). In-situ polymerized cellulose nanocrystals (CNC)-poly(l-lactide) (PLLA) nanomaterials and applications in nanocomposite processing. *Carbohydrate Polymers*, *153*, 549-558.

Moon, R. J., Martini, A., Nairn, J., Simonsen, J., & Youngblood, J. (2011). Cellulose nanomaterials review : Structure, properties and nanocomposites. *Chemical Society Reviews*, *40*, 3941-3994.

Morandi, G., Piogé, S., Pascual, S., Montembault, V., Legoupy, S., & Fontaine, L. (2009). ATRP and ROMP : Modular chemical tools for advanced macromolecular engineering. *Materials Science and Engineering: C*, *29*, 367-371.

Morandi, Gaelle, Heath, L., & Thielemans, W. (2009). Cellulose Nanocrystals Grafted with Polystyrene Chains through Surface-Initiated Atom Transfer Radical Polymerization (SI-ATRP). *Langmuir*, *25*, 8280-8286.

Natterodt, J. C., Petri-Fink, A., Weder, C., & Zoppe, J. O. (2017). Cellulose Nanocrystals : Surface Modification, Applications and Opportunities at Interfaces. *CHIMIA International Journal for Chemistry*, *71*, 376-383.

Nechyporchuk, O., Belgacem, M. N., & Bras, J. (2016). Production of cellulose nanofibrils : A review of recent advances. *Industrial Crops and Products*, *93*, 2-25.

Nyström, D., Lindqvist, J., Östmark, E., Hult, A., & Malmström, E. (2006). Superhydrophobic bio-fibre surfaces via tailored grafting architecture. *Chem. Commun.*, *34*, 3594-3596.

Oksman, K., Aitomäki, Y., Mathew, A. P., Siqueira, G., Zhou, Q., Butylina, S., Tanpichai, S., Zhou, X., & Hooshmand, S. (2016). Review of the recent developments in cellulose nanocomposite processing. *Composites Part A: Applied Science and Manufacturing*, *83*, 2-18.

Park, S., Baker, J. O., Himmel, M. E., Parilla, P. A., & Johnson, D. K. (2010). Cellulose crystallinity index : Measurement techniques and their impact on interpreting cellulase performance. *Biotechnology for Biofuels*, *3*, 1-10.

Reid, M. S., Villalobos, M., & Cranston, E. D. (2016). Benchmarking cellulose nanocrystals : From the laboratory to industrial production. *Langmuir*, *33*, 1583–1598.

Robles, E., Urruzola, I., Labidi, J., & Serrano, L. (2015). Surface-modified nano-cellulose as reinforcement in poly(lactic acid) to conform new composites. *Industrial Crops and Products*, *71*, 44-53.

Sabatini, D. M. (2007). *Leading Edge Nanotechnology Research Developments*. Nova Publishers.

Segal, L., Creely, J. J., Martin, A. E., & Conrad, C. M. (1959). An Empirical Method for Estimating the Degree of Crystallinity of Native Cellulose Using the X-Ray Diffractometer. *Textile Research Journal*, *29*, 786-794.

Sessini, V., Navarro-Baena, I., Arrieta, M. P., Dominici, F., López, D., Torre, L., Kenny, J. M., Dubois, P., Raquez, J.-M., & Peponi, L. (2018). Effect of the addition of polyester-grafted-cellulose nanocrystals on the shape memory properties of biodegradable PLA/PCL nanocomposites. *Polymer Degradation and Stability*, *152*, 126-138.

Siqueira, G., Bras, J., & Dufresne, A. (2010a). New Process of Chemical Grafting of Cellulose Nanoparticles with a Long Chain Isocyanate. *Langmuir*, *26*, 402-411.

Siqueira, G., Bras, J., & Dufresne, A. (2010b). Cellulosic Bionanocomposites : A Review of Preparation, Properties and Applications. *Polymers*, *2*, 728-765.

Tian, C., Fu, S., Habibi, Y., & Lucia, L. A. (2014). Polymerization Topochemistry of Cellulose Nanocrystals : A Function of Surface Dehydration Control. *Langmuir*, *30*, 14670-14679.

Viet, D., Beck-Candanedo, S., & Gray, D. G. (2007). Dispersion of cellulose nanocrystals in polar organic solvents. *Cellulose*, *14*(2), 109-113. https://doi.org/10.1007/s10570-006-9093-9

Wang, X., Jing, S., Liu, Y., Qiu, X., & Tan, Y. (2017). Preparation of dithiocarbamate polymer brush grafted nanocomposites for rapid and enhanced capture of heavy metal ions. *RSC Advances*, *7*, 13112-13122.

Xiao, M., Li, S., Chanklin, W., Zheng, A., & Xiao, H. (2011). Surface-initiated atom transfer radical polymerization of butyl acrylate on cellulose microfibrils. *Carbohydrate Polymers*, *83*, 512-519.

Zhang, Z., Tam, K. C., Sèbe, G., & Wang, X. (2018). Convenient characterization of polymers grafted on cellulose nanocrystals via SI-ATRP without chain cleavage. *Carbohydrate Polymers*, *199*, 603-609.

Zhou, L., He, H., Li, M.-C., Huang, S., Mei, C., & Wu, Q. (2018). Grafting polycaprolactone diol onto cellulose nanocrystals via click chemistry : Enhancing thermal stability and hydrophobic property. *Carbohydrate Polymers*, *189*, 331-341.

Zoppe, J. O., Habibi, Y., Rojas, O. J., Venditti, R. A., Johansson, L.-S., Efimenko, K., Österberg, M., & Laine, J. (2010). Poly(N-isopropylacrylamide) Brushes Grafted from Cellulose Nanocrystals via Surface-Initiated Single-Electron Transfer Living Radical Polymerization. *Biomacromolecules*, *11*, 2683-2691.

Zoppe, J. O., Xu, X., Känel, C., Orsolini, P., Siqueira, G., Tingaut, P., Zimmermann, T., & Klok, H.-A. (2016). Effect of Surface Charge on Surface-Initiated Atom Transfer Radical Polymerization from Cellulose Nanocrystals in Aqueous Media. *Biomacromolecules*, *17*, 1404-1413.